Sustainable and cost-effective MAS DNP-NMR at 30 K with cryogenic sample exchange

Subhradip Paul, Eric Bouleau, Quentin Reynard-Feytis, Jean-Pierre Arnaud, Florian Bancel, Bertrand Rollet, Pierre Dalban-Moreynas, Christian Reiter, Armin Purea, Frank Engelke, et al.

Sustainable and cost-effective MAS DNP-NMR at 30 K with cryogenic sample exchange

Subhradip Paul [a], *Eric Bouleau* [b], *Quentin Reynard-Feytis* [a], *Jean-Pierre Arnaud* [b], *Florian Bancel* [b], *Bertrand Rollet* [b], *Pierre Dalban-Moreynas* [b], *Christian Reiter* [c], *Armin Purea* [c], *Frank Engelke* [c], *Sabine Hediger* [a], *Gaël De Paëpe* [a]*

[a] Univ. Grenoble. Alpes, CEA, CNRS, IRIG, MEM, 38000 Grenoble, France

[b] Univ. Grenoble Alpes, CEA, IRIG, DSBT, 38000 Grenoble, France

[c] Bruker Biospin 76275 Ettlingen, Germany

Abstract We report here instrumental developments to achieve sustainable, cost-effective cryogenic Helium sample spinning in order to conduct dynamic nuclear polarisation (DNP) and solid-state NMR (ssNMR) at ultra-low temperatures (< 30 K). More specifically, we describe an efficient closed-loop helium system composed of a powerful heat exchanger (95% efficient), a single cryocooler and a single helium compressor to power the sample spinning and cooling. The system is integrated with a newly designed triple-channel NMR probe that minimizes thermal losses without compromising the RF performance and spinning stability (+/- 0.05%). The probe is equipped with an innovative cryogenic sample exchange system that allows swapping samples

in minutes without introducing impurities in the close-loop system. We report that significant gain in sensitivity can be obtained at 30-40 K on large micro-crystalline molecules, with unfavorable relaxation timescales, making them difficult or impossible to polarize at 100 K. We also report rotor-synchronized 2D experiments to demonstrate the stability of the system.

Magic angle spinning (MAS) solid-state NMR at high magnetic field has developed as a key spectroscopy to study the structure and dynamics of a wide array of systems including bio-solids, catalysts, drugs, and energy materials [1–5]. Nevertheless, there are still emerging applications, both for biomolecules (*in vitro* and *in cell* NMR), small molecules and materials (bulk and especially surfaces), where NMR still suffers from its relatively limited sensitivity[6–9].

Besides the access to stronger magnetic field, such limitations can be strongly attenuated by cooling the electronics of the probe [10] and/or the sample to cryogenic temperatures [11,12], but also by hyperpolarizing the sample by Dynamic Nuclear Polarization (DNP) through microwave (μw) irradiation. The latter involves the transfer of polarization from unpaired electrons to the nuclei of interest and is driven by the application of a suitable microwave irradiation [13–15]. The recent renaissance of DNP and its combination with high magnetic field and sample spinning is a direct consequence of the groundbreaking research undertaken by the Griffin group at Massachusetts Institute of Technology (MIT) [16–18]. Since then, a growing community of DNP practitioners has reported a large range of previously infeasible applications, further increasing the impact of DNP and revolutionizing the scope of solid-state NMR [19–27]. These advances are supported by theoretical insights [28–37], as well as the development of innovative hardware [18,38–41] and biradical polarizing agents [42–45].

The last decade has witnessed the introduction of new polarizing agents (PAs), in particular for high field and fast MAS experiments [46–55]. The last generation of PAs have improved significantly the sensitivity, with ^{1}H DNP enhancement factors (compared to Boltzmann polarization) at 100 K typically around 50 to 200 (depending on the rotor diameter) and buildup times between 1s to 10 s depending on the magnetic field and the system to polarize. To improve things further, the development of new PAs can be combined with performing DNP experiments

at temperatures much lower than 100 K. Several initiatives aiming at developing ultra-low temperature MAS experiments have been reported and have recently been reviewed [11,12,39,40,56]

Except for the system built at NIH in Tycko's group [56] that uses cold nitrogen gas (N_2) to spin the sample and cold helium gas to cool the sample down to 20 K, most of the recent reports relied on the use of Helium for both spinning and cooling the sample. The approach was pioneered by Yannoni and coworkers, and more recently implemented in the Barnes group that showed the possibility to spin the sample down to 5 K [57,58] using nitrogen-cooled helium gas and liquid He blowing on the center of the rotor. In 2012 – 2013, the group of Fujiwara [59] and Levitt [12] showed results down to < 25 K using pressurized LHe dewar for spinning and cooling.

In 2015, a milestone was achieved by the Osaka and Grenoble groups, demonstrating the use of helium closed-loop systems based on the use of gas compressors and counter-flow heat exchangers to achieve stable sample rotation and cooling [60,61]. The Grenoble group could demonstrate a factor of ~30-50 in time-savings on self-assembled peptide nanocrystals using TOTAPOL by lowering the sample temperature from 100-110 K to the 40-50 K range under DNP condition [61]. Also, using a 3.2 mm rotor, faster sample spinning was demonstrated with He (17.5 kHz at 50 K) than N_2 (12.5 kHz at 108 K). Finally, 100 kHz ^{1}H decoupling was reported over 50 ms acquisition without arcing. This first experimental setup (called NUMOC) used LHe to cool the Bearing, Drive, and VT (variable temperature) gas flows, using a single compressor and powerful heat exchanger for all three lines. On the other hand, the Osaka group was able to fully remove the use of LHe and to reach 4 kHz MAS at 35 K and 4.7 kHz at 40 K using two GM cryo-coolers (one for the Bearing and one for the Drive) [60]. Afterwards, they were able to combine this setup with

DNP and access faster MAS and lower temperature (10 kHz at 22 K) by adding three additional cryo-coolers [40].

In recent years, we have continued developing our system in Grenoble with the goal to make it sustainable, in terms of Helium consumption, and cost-effective, in terms of hardware and cooling power requirement, without compromising on the RF, μw, and MAS capabilities. To reach this goal, we have designed an improved cryostat that relies on the use of a single cryocooler and a single compressor for all three Bearing, Drive, and VT lines, and a new generation of triple channel DNP probe that truly acts as a helium-tight cryostat providing excellent thermal insulation. The latter is also equipped with a cryogenic sample exchanger that allows switching samples in minutes without warming up and opening of the probe. Beyond the convenience for day-to-day usage, this is also an extremely important point for setting reliably the stator at the magic angle once the probe is cold (30-40 K). Indeed, the angle may need to be slightly readjusted between temperature cycles, although this is not always the case with the current probe. A nutation frequency of 100 kHz on the ^{1}H channel is achieved using 76.3 W of power at 40 K, whereas 62.5 kHz ^{13}C using 50 W. Combined with cAsymPol-POK, one of the latest generation of PA that we have recently introduced, we can improve the signal-to-noise ratio for proton-dense methyl-containing organic powdered sample [50,54] by a factor 5 to 23 by lowering the sample temperature from 100 K to 40 K. We also illustrate the reliability of the setup regarding RF performance and sample spinning stability, by showing 2D DQ-^{13}C^{13}C-^{13}C SR26 and ^{15}N-^{13}C TEDOR experiments performed on diluted ^{13}C,^{15}N-*f*-MLF.

MATERIALS AND METHODS

Sample preparation for DNP

The ampicillin and indomethacin samples were purchased from Sigma-Aldrich and used as is for the preparation of DNP sample. 37 mg of each were ground to a fine powder and impregnated with 10 µl of 20 mM cAsymPol-POK in d8-Glycerol/D_2O/H_2O 60:30:10 (v:v:v) (GDH matrix).

For the *f*-MLF tripeptide, one part of ^{13}C-^{15}N isotopically labelled tripeptide (4 mg) and four parts of unlabeled peptide (16 mg) were co-dissolved in isopropanol and recrystallized following the protocol in Ref [62]. KBr (10 mg) was added to the sample to be used as internal thermometer [63]. The sample was impregnated with 15 µl of 10 mM cAsymPol-POK in GDH matrix.

DNP-enhanced solid-state NMR experiments

Solid-state NMR experiments were recorded using a Bruker DNP-NMR AVANCE III 400 MHz (9.4 T) spectrometer equipped with a gyrotron (operating at its fundamental mode) and a corrugated transmission line. For all the DNP experiments, the µw power was about ~15-21 W, measured at the probe base using a water load (before the taper). All the DNP-NMR measurements were performed with a home-built 3.2 mm HXY triple-resonance MAS probe that can be operated at cryogenic temperature and is suitable for Helium spinning. The field of the 9.4 T magnet was slightly adjusted such that the microwave irradiation at 263.7 GHz was matching the maximum intensity in the AsymPol-POK's field profile, resulting in ^{1}H resonating at 400.2 MHz, ^{13}C at 100.6 MHz on the X-channel, and ^{15}N at 40.6 MHz on the Y channel of the probe (set in triple channel configuration).

NMR parameters

Cross Polarization experiments

The 1D experiments at 100 K and 40 K were carried out at a spinning frequency (ν_r) of 8 kHz. For each experiment, 15 ms of free induction decay and 128 transients were acquired. The spectra were processed with Topspin without any apodisation and plotted using Nmrglue [64] and Python. The referencing was done indirectly with respect to TMS using adamantane at room temperature. All the experimental parameters are tabulated in Table 1 of the supplementary information.

DARR

The DARR [65] experiment was carried out at 40 K with $\nu_r = 7.5$ kHz. 25 ms of acquisition time was employed in the direct dimension with 2.6 s of recycle delay between the 4 transients of each indirect time increment. 256 slices (128 complex points) were collected in the indirect dimension. The slices were collected using STATES-TPPI for quadrature detection, with a spectral width of 250 ppm. For DARR, the mixing time was set to 20 ms with an RF field strength on ^{1}H matching the spinning frequency. The experimental parameters are tabulated in Table 2 of the supporting information.

z-filtered TEDOR

The *z*-filtered TEDOR experiment was carried out at 40 K with ν_r = 7 kHz. The REDOR mixing period was set at 1.14 ms to favour polarization transfer over distances corresponding to one-bond. A z-filter of one rotor period was used to obtain purely absorptive peaks [66]. 16 transients were collected with 2.6 s recycle delay for each increment. 96 slices (48 complex points) were collected in the indirect dimension using STATES-TPPI with a spectral width of 40 ppm. The experimental parameters are tabulated in Table 2 of the supporting information.

DQ-SQ correlation

The experiment was carried out at 40 K at ν_r= 6.7 kHz. Modified SR26 recoupling [67] with STiC phase-shift [68] was used for 4.77 ms total mixing time (double-quantum excitation and reconversion). During the recoupling periods, 100 kHz Lee-Goldburg continuous wave decoupling was applied to remove both ^{1}H-^{13}C and ^{1}H-^{1}H couplings. For each increment, 16 scans were recorded with 2.6 s recycle delay. 128 slices (64 complex points) were recorded in the indirect dimension using STATES-TPPI with a spectral width 400 ppm. The experimental parameters are tabulated in Table 2 of the supporting information.

RESULTS AND DISCUSSION

Compared to the results reported earlier [39,61], our 3.2 mm MAS-DNP probe (called PAVLOT) was completely re-designed to make it suitable for operation at ultra-low temperature in a sustainable and cost-effective fashion. With the same purpose, our closed-loop cooling system was upgraded for better performances and to fully eliminate helium consumption. The key modifications made to the different parts of the system as well as specifications and results obtained are delineated below.

Probe dewar architecture

The probe was designed as a small cryostat and consists of two main parts, a probe base and a cylindrical part (probe tube) that goes inside the magnet (Fig. 1). The interior of the probe tube, which includes the stator, the RF capacitors and the internal waveguide, is maintained in a cold helium atmosphere. The latter space is thermally isolated from the laboratory thanks to a double-walled tubular envelope maintained under vacuum. To minimize thermal losses, the outer tube can

159 be clamped to the probe base housing without any contact with the inner tube, which contains the
160 cold gas. The inner tube can withstand a pressure of 4 bar on the inside while a vacuum is applied
161 on its outside (2×10^{-5} mbar), between the two walls.

162 The base of the probe is also under vacuum, to minimize thermal loss (5×10^{-6} mbar). This is
163 mandatory if one wants to minimize the number of cryocoolers needed to cool the closed-loop He
164 cycle. This is very different from a conventional 100 K DNP probe, where the probe base is
165 deliberately kept at higher temperature using flush gas to avoid freezing and condensation. This
166 latter approach is compatible with reaching 100 to 110 K at the sample using liquid nitrogen
167 cooling. This is obviously no longer suitable at helium temperatures, and for that reason we
168 designed our probe base as a small cryostat with the inner part protected from ambient temperature
169 by vacuum.
170

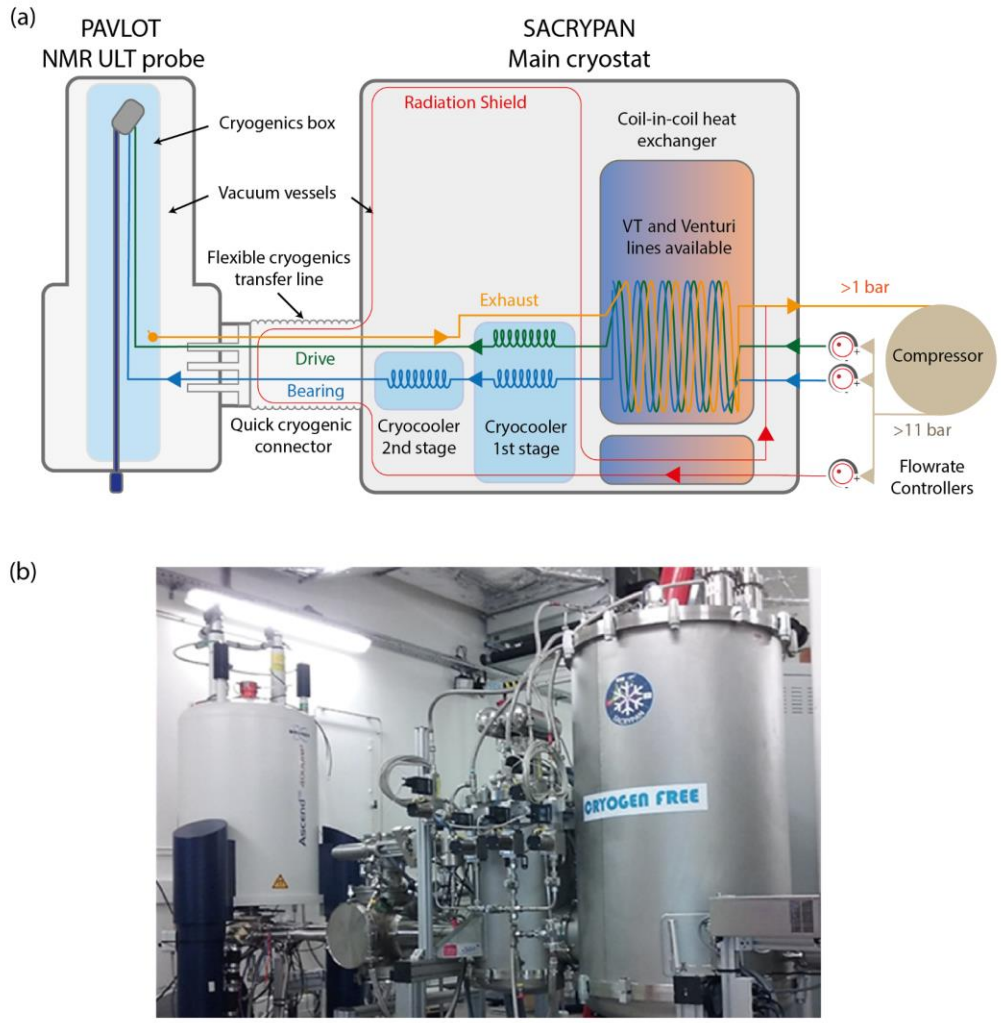

Figure 1. (a) Schematic of the closed-loop helium spinning system built at CEA Grenoble (b) Corresponding photograph of the system, the probe being in the NMR magnet bore.

Closed-loop He cycle for Bearing/Drive/VT gas powered with a single compressor

As described previously [39,60,61], the rotation and cooling of the sample is achieved via a closed-loop helium cycle. In our case, the system is built around a single water-cooled screw compressor (Quantum systems – L x W x H = 0.8 x 0.6 x 1 m; Power rating = 11 kW) which can deliver a gas flow rate up to 1286 l/min (mass flow rate of 3.4 g/s) and create a pressure up to 11 bar. The compressor is equipped with two 100-litre buffer gas tanks on the high- and low-pressure inlets respectively. Helium gas is compressed to a pressure of 9 bar and then fed into a cabinet that

controls the flow of four independent streams. The first two lines are used for sample spinning (i.e. bearing and drive). The third line can be used for sample cooling (VT line) or, in the future, as a Venturi line for 1.3 or 0.7 mm diameter rotor. The fourth line cools the radiation shield of the cryostat, which contains the heat exchanger. We use additional 10 l buffer tanks (located before the exchanger) on the bearing and drive lines to minimize fluctuations in sample spinning and to act as a damper in case of compressor failure. The set up allows us to achieve a sample spinning stability of 0.05 % (see Fig. 2a). The spinning detection is done using fiber optics and a home-built spinning detection module. Currently the sample spinning is performed by setting manually the Bearing and Drive flowmeter target values, which are regulated by feedback control. Automated control of the spinning frequency using feedback loops on the drive and bearing flows will be implemented soon.

The low-pressure tank on the compressor is maintained at 1.1 bar. Since we are working with a closed-loop He cycle, this pressure corresponds also to the pressure inside the probe, which is maintained above atmospheric pressure. After passing through the stator to spin the rotor, the helium gas is deflected down the probe using a Kapton wrap, generating a persistent gas flow around the capacitors. The high flow and high pressure inside the probe helps to prevent arcing [60,61].

Coupling the probe to the cryostat

Cold He gas streams are delivered to the probe using a flexible cryogenic line, which is both under vacuum (10^{-5} mbar) and thermally shielded (< 110 K). The connection ports to the probe are Johnston bayonet type fittings. The five pairs of insulated tubes (bearing, drive, VT, radiation

shield, venturi) are equipped with a specific gasket to obtain a very good cold seal. The clamp can withstand pressures up to several bars and is easily installed in less than a minute with toggle locks.

The initial cooling time of the entire setup, the cryostat and the probe, from RT to 30 K, measured at the sample, is less than 24 h. We typically use < 500 L of He (under Normal Temperature and Pressure) to flush the system before cooling. During normal system operation (i.e. under MAS), there is virtually no helium consumption. The probe can be detached from the main cryostat within 30 minutes. While the probe is disconnected, the cryostat can be isolated and kept cold using a flexible 5-line isolation loop. The probe can be reconnected and cooled down in 30 minutes due to its low heat capacity and good thermal insulation. Overall, this procedure consumes < 100 L of He (under Normal Temperature and Pressure). This is particularly convenient for changing the probe configuration without warming up the entire system.

Powerful heat exchanger equipped with a single cryocooler for cost-effective He spinning

As previously reported, we use a counter-flow heat exchanger that has been designed to achieve a perfect balance. The length of the helical coil-in-coil multi-tubes of the exchanger is calculated so that the counter-flow heat exchange process takes most of the energy out of the gas entering the exchanger, which implies that the out-going gas at the inlet point of the exchanger has temperature close to that of the incoming gas. The efficiency of the heat exchanger can be expressed as follows:

$$E \approx \frac{T_{1,in} - T_{1,out}}{T_{1,in} - T_{2,in}}$$

where, $T_{1,in}$ and $T_{2,in}$ are the temperatures of the two incoming gas flow, $T_{1,out}$ is the temperature of the gas flow 1 at the outlet of the tube-in-tube architecture. When the mass flow rates of the two gases are equal, the efficiency of the counter-flow heat exchange process can be conveniently related to the Number of Transferrable Units (NTU):

$$NTU = \frac{E}{1 - E}$$

NTU is a dimensionless constant which depends on the surface area available for exchange. Three configurations of heat exchanger were tested corresponding to NTU of 19, 24, and 32, which translate into 95 %, 96 %, and 97 % of transfer efficiency. The 96 % and 97 % configurations allow reducing the sample temperature by 4 K and 7 K, respectively, with respect to the 95 % one. However, they both result in a significant drop in pressure that is detrimental for fast sample spinning. Therefore, we chose to work with 95 % efficiency in this study. The design of the exchanger was guided by numerical calculations with three aims in mind: (a) to transfer most of the enthalpy from the outgoing to the incoming gas, (b) to minimize the pressure drop through the heat exchanger to favor high spinning frequencies while minimizing frictional heat inside the tubes, (c) to minimize longitudinal conduction along the tubes to produce a thermal by-pass, which prevents heat conduction from the warm to the cold end.

After passing through the heat exchanger, the He gas goes through a two-stage CRYOMECH PT cooler that can reach 10 K in one hour. The first stage produces 80 W of cooling power at 55 K while the second stage provides 22 W of cooling power at 18 K. The compressor of the PT requires 9.2 kW and can be stored easily because of the relatively small footprint (L x W x H = 0.6 x 0.6 x 0.6 m). Each of the cryocoolers used in the OSAKA setup (i.e. 3 to 5 GM) have similar performance as the unique PT cryocooler used here, highlighting both the excellent performance of our heat exchanger and the minimal losses of the system (cryostat and probe). The CRYOMECH cryocooler is mechanically connected to 2 regenerative heat exchangers, also known as capacitive heat exchangers, which consist of a single flow path inside a copper block to temper the fluid. The capacitive heat exchangers are mounted with the goal to minimize thermal resistance (0.01 K/W). Three heat exchanger configurations were tested for cryogenic Helium spinning:

1. Drive, bearing, and VT gas lines going through the first stage of the cryocooler and only the VT line further through the second stage. In this configuration, we could reach about 50 K at the sample.
2. Drive, bearing, and VT gas lines all going through the first stage of the cryocooler and both bearing and VT lines further through the second stage. With this configuration, we could reach 40 K at the sample.
3. Drive and bearing gas lines going through the first stage of the cryocooler and only the bearing line further through the second stage. No VT gas is used. With this configuration, we could reach 30 K on the sample.

We conclude that for 3.2 mm rotor and our current setup, there is no need to use a VT line. The sample temperature was measured using a rotor filled with KBr and spinning the sample at 8 kHz [63]. Note that 20 W μw irradiation (measured at the probe base) increases the sample temperature by ~5 K for a zirconia rotor filled with KBr.

Probe performances: spinning stability, noise figure, and RF field strengths

The spinning stability of our system was monitored by following the position of the first sideband of a series of ^{79}Br spectra. As each spectrum can be recorded with only one scan, it provides a direct access to frequency fluctuations of our system. As shown in Fig. 2a, we monitored the position of the sideband every 2 s, over a period of about 45 min. The variation in spinning frequency is about 0.05% of the nominal value, indicating an excellent stability, which is important for conducting experiments that demand rotor synchronization and spinning stability.

The current setup allows reaching 27 K at low spinning speed (~5 kHz) and in absence of microwave irradiation. The rotors can be spun up reliably up to 10 kHz at 30-35 K in absence of

microwave irradiation. The latter increases the temperature of standard samples by 5-7 K using the full power of the gyrotron (about 22 W at the base of the probe).

In order to provide best sensitivity, it is mandatory to investigate the noise level of the probe. At helium temperature, the probe circuit can act as a good receiver to pick up RF signals from surrounding electromagnetic waves and from other electronic circuits in proximity (temperature sensors, MAS detection, etc.). In Fig. 2b, the blue trace shows the initial noise spectrum obtained for PAVLOT at 40 K with the X channel tuned to ^{13}C. It clearly demonstrates the undesirable RF pickup of FM radio broadcasting. After shielding and grounding of the probe connectors and internal components (mainly the Cernox sensor used for the detection of the sample temperature), the noise spectrum was significantly improved at 40 K (orange trace). Considering the specific frequency region of the carbon spectra (0 – 200 ppm), the noise is reduced by a factor of 1.5 going from 298 K to 40 K (comparison between green and orange data). With an electronic circuit (probe and preamplifier) entirely cooled, one would expect the thermal noise to improve by a factor of ~2.8 by going from 298 to 40K. We ascribe the discrepancy to the fact that the pre-amplifier is not cooled here. This strongly support the development of cold preamplifier for NMR experiments run at ultra-low temperature, as recently demonstrated by Matsuki *et al*.[69].

As mentioned previously, we maintain high flow and pressure in the probe to avoid any arcing. This approach seems so far successful as demonstrated in Fig. 2c, which shows the free induction decay (FID) of a CP experiment acquired with 25 ms of ^{1}H decoupling at 100 kHz rf field strength. Nutation curves on both ^{1}H and ^{13}C channels are given in Fig. 2d at RF field strengths of 78.1 kHz (at 60 W) and 62.5 kHz (at 50 W), respectively. The ^{1}H nutation curve was recorded indirectly through CP by detecting ^{13}C while increasing the length of the ^{1}H excitation pulse, giving maximum signal intensity for a 90° pulse. The carbon nutation curve was recorded by increasing

the length of a flip-back pulse after the CP, resulting in a zero-crossing of the signal intensity for the 90° pulse.

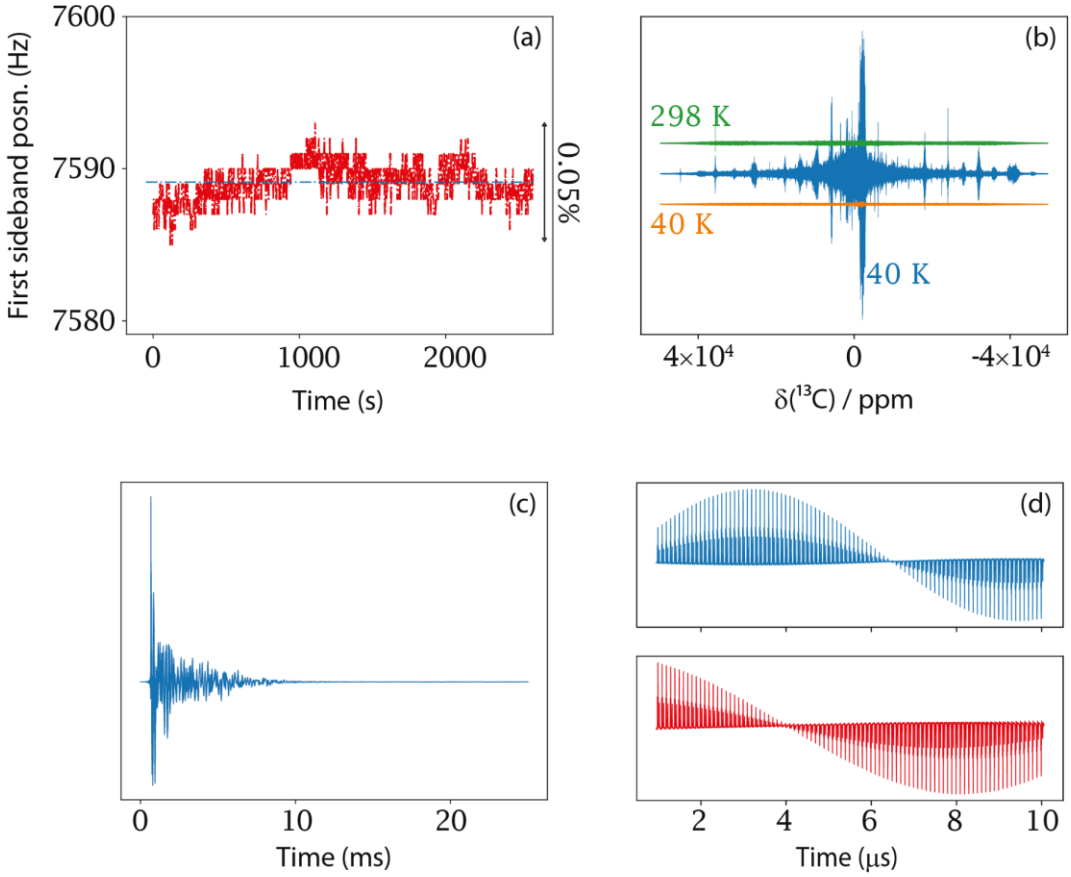

Figure 2 (a) Position of the 1st sideband, with respect to the centerband, in a ^{79}Br spectrum of KBr. The spectrum was recorded with 1 scan every 2 s. The nominal spinning frequency was 7589 Hz, and the maximum variation observed was 0.05% of the nominal frequency as indicated. (b) Noise spectra acquired with a large spectral window at 40 K before shielding and grounding (blue) and at 298 K (green) / 40 K (orange) after shielding of the probe components. (c) ^{13}C FID acquired for 25 ms with 100 kHz ^{1}H decoupling. (d) Nutation experiments performed indirectly via CP on ^{1}H (top panel), and ^{13}C (bottom panel). The corresponding nutation frequency are 78.1 kHz at 60 W for ^{1}H, and 62.5 kHz at 50 W for ^{13}C (3.2 and 4 µs 90° pulse for ^{1}H and ^{13}C, respectively).

RF circuit and matching/tuning capability

The RF part of the probe is a commonly used triple resonance configuration, consisting of a transmission line in the 1H channel and lumped elements such as variable capacitors and inductances for tuning, matching and providing isolation between channels. The variable

capacitors consist of two coaxial sapphire cylinders with variable overlap. Using the same material for the inner and outer part of the capacitor allows for tuning in a wide temperature range, preventing any mechanical jamming due to different thermal expansion coefficients. Hence, the coil and the RF capacitors are placed in the cold He environment consistent with our previous design, which also leads to an improvement in signal-to-noise ratio due to lower thermal noise.

The X and Y tuning capacitors feature a capacitance range of 2 to 50 pF, giving both channels broadband capabilities. By adding shunt capacitors in parallel to the tuning capacitors, the range can be further extended towards lower frequencies, whereas a serial capacitor can be connected to increase the X and Y frequencies, and the XY stop circuit can be changed to implement various triple resonance configurations. The RF circuit is not optimized for one fixed set of nuclei but is kept flexible to enable tuning to multiple nuclei. A proper isolation between the different RF channels is done by LC stop circuits and grounding at the zero voltage crossing along the transmission line.

It is important to stress that the probe behaves like a small helium-tight cryostat, which imposes new constraints, such as the design of helium-tight cryogenic feedthroughs that control the cold RF capacitors and the magic angle setting. The probe shown in Fig. 3 is equipped with 7 cryogenic feedthroughs corresponding to the tuning/matching capacitors for the three HXY channels and the magic angle adjustment system.

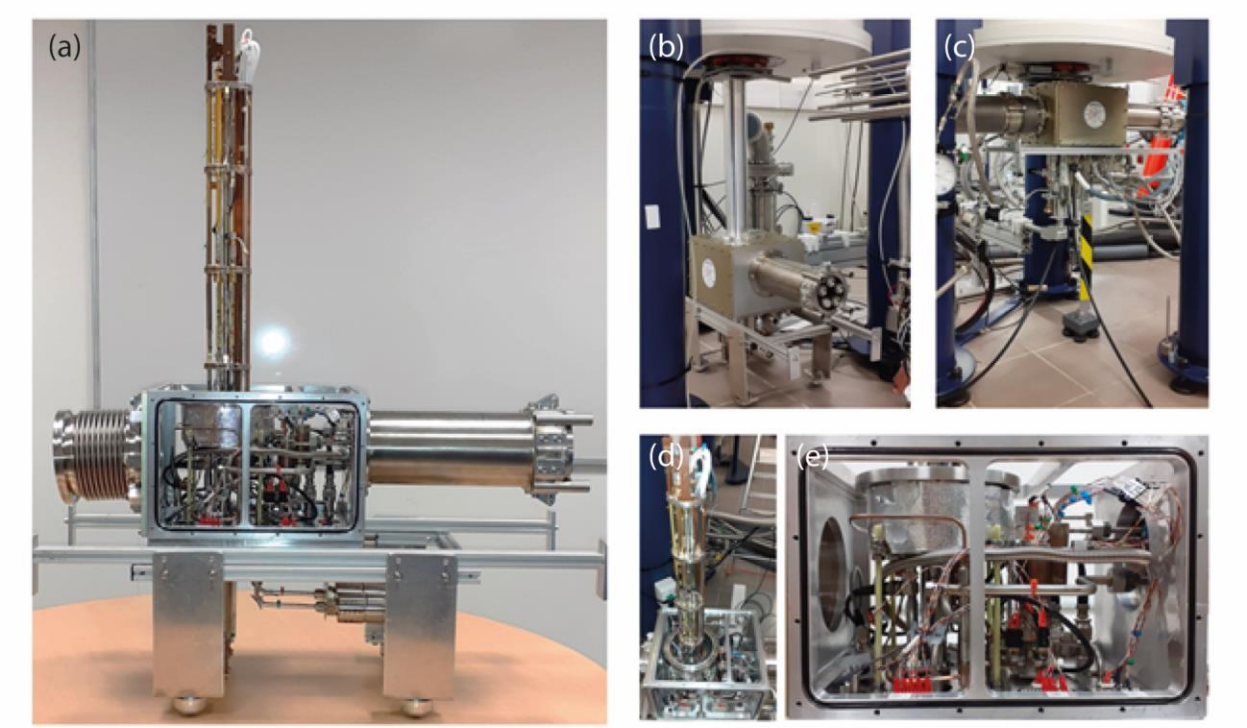

Figure 3. (a) Profile of our re-designed probe. (b) and (c) Photograph of the probe being inserted in a wide-bore 9.4 T magnet. (d) Top view of the RF circuits with (e) zoom on the tuning and matching rod feedthroughs.

Cryogenic sample exchange compatible with a helium closed loop cycle

To prevent any pollution of the closed-loop He cycle, e.g. seeping moisture, which would cause spinning problems or rotor blockage in the transfer line, we conceived an antechamber fixed at the sample insert/eject point of the probe. Before inserting a sample, the rotor is placed in a home-built sample-catcher acting as antechamber, and three cycles of helium gas flushing and subsequent pumping (two minutes) are performed. To our knowledge, this is the first example of an insert-eject system that is compatible with a closed-loop He-spinning system. This is an important step towards routine use of such a technology. Indeed, the absence of cryogenic sample exchange implies to warm up, disconnect, and open up the probe before the sample can be exchanged. Then, the probe needs to be reconnected and cooled down again. The cooling of the probe is then done while spinning the sample from RT to cryogenic temperature (20 to 40 K

typically) [60]. Overall, such a procedure is time-consuming, tedious and has a high probability of introducing impurities into the probe and therefore into the recirculated closed-loop system. With the cryogenic insert-eject system described here, the sample is inserted into the cold probe within minutes, ready to be spun and measured. Overall, inserting/ejecting a sample requires about 1 L of He gas (at Normal Temperature and pressure).

Furthermore, this insert-eject system enables refining the magic angle (if needed) at the experimental cryogenic temperature prior to start experiments. Without this system, one needs to warm up the entire probe after magic-angle setting, e.g. using KBr, to insert the sample of interest before cooling back again. Such important temperature cycles of ~250 K can sometimes slightly change the magic angle settings, making it unreliable.

Sensitivity considerations at 100 K and below

As reported in the literature, there is a clear interest in performing MAS NMR at cryogenic temperatures of 100 K and below, and combining it with DNP, when possible. In addition to increasing the spin polarization, cooling the sample and probe electronics also reduces noise [60,61,70], both improving the signal-to-noise ratio (SNR). Additionally, cooling the sample to cryogenic temperatures also lengthens nuclear coherence dephasing times, which allows for significantly increased polarization transfer. This has proven particularly useful in the case of quadrupolar nuclei and to record long-distance ^{13}C-^{13}C and ^{15}N-^{13}C transfer at natural isotopic abundance [20,71–76].

Recently, several groups have combined DNP at temperature much lower than 100 K. In all cases, these reports have pointed towards a systematic gain in sensitivity, typically up to one order of magnitude, by reducing the sample temperature from 100 K to 30 K, depending on the

systems and PA used [39,56,61,69,77,78]. This was also tested with our new probe and is discussed in the next paragraph (see also Fig. 4).

Polarizing protonated microcrystals with DNP at << 100 K

As recently reported by our group [54], it is important to report the performance in sensitivity of polarizing agents on protonated systems and not simply on deuterated frozen solutions. Therefore, we chose two proton-dense microcrystalline solids impregnated with cAsymPol-POK, one of the latest polarizing agents reported so far [50]. Organic microcrystals are non-porous micrometer-size particles. Polarizing microcrystals with DNP is challenging but can be facilitated if one of the crystal dimensions (or more) is smaller than a micron, or if the ^{1}H bulk longitudinal relaxation time constant T_{1n} of the undoped system is much longer than the time needed to propagate the hyperpolarization from the outer shell to the core of the system [79–81].

To illustrate the benefits in lowering the sample temperature down to 30-40 K, we chose to polarize two organic microcrystals, ampicillin and indomethacin, that have an inherent bulk ^{1}H T_{1n} (undoped) of > 70 s and ~ 3s, respectively, at 100 K. Since it typically takes a few seconds (or more) to polarize microcrystals with DNP at 100 K and 9.4 T, the very short bulk ^{1}H T_{1n} of indomethacin makes it extremely difficult to polarize compared to ampicillin, which has a longer bulk ^{1}H T_{1n} of > 70 s.

The results are reported in Fig. 4, which shows the ^{13}C signal-to-noise (SNR) as a function of the hyperpolarization time, at 100 K and 40 K. The ^{13}C signal is measured through ^{1}H to ^{13}C CPMAS. The obtained buildup curves can be fitted using one or two exponential functions. For the build ups requiring two components, the shorter of the two is directly related to the efficiency of the PA to polarize the outer shell of the particles (about hundreds of nm)[79], whereas the longer

component can be seen as the ability to polarize the nuclei at the core which are more distant from the polarizing agent [46,54,73,73,76,81].

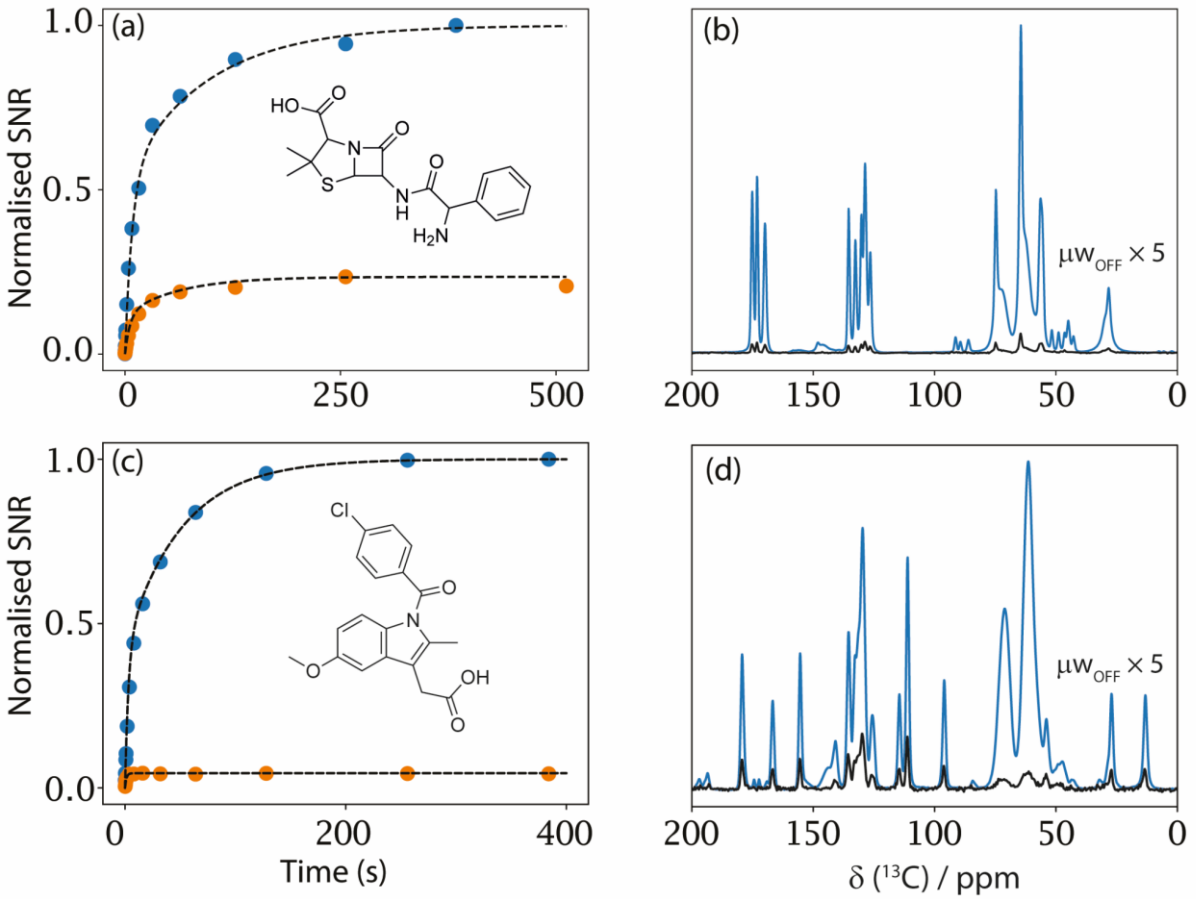

Figure 4. (a) and (c) Signal to noise (SNR) ratio as a function of the hyperpolarization time (DNP build up experiments) at 100 K (orange circles) and 40 K (blue circles) of (a) the C11 resonance of ampicillin at 172 ppm and (c) the C10' of indomethacin at 155.1 ppm. SNR was measured from ^{1}H-^{13}C CP spectra. The samples were impregnated with 20 mM cAsymPol-POK in GDH matrix (see Materials and Methods). The polarization buildups were fitted with a sum of two exponentials as described in the text, except for the indomethacin one at 100 K, which is mono-exponential. (b) and (d) Microwave on (blue) and microwave (off) (black and scaled vertically by a factor 5) CPMAS spectra at 40 K of (b) ampicillin with a recycle delay of 11.2 s and (d) indomethacin with a recycle delay of 5 s. The recycle delay was calculated in each case to obtain the best sensitivity [54]. The apparent DNP enhancement factor $\varepsilon_{on/off}$ is about 98 for ampicillin and 23 for indomethacin. For the CP experiments, 81 kHz of ^{1}H decoupling using SW$_f$-TPPM [82,83] was applied during detection. Ramped CP of 2 ms contact time was used to transfer the polarization from the ^{1}H to ^{13}C [84]. Pre-saturation pulses were used on both channels and an echo of two rotor-periods in all was applied prior to detection.

For the ampicillin sample, we first notice that the SNR at the plateau is increased by a factor of 4.8 by lowering the temperature from 100 K to 40 K. For a better understanding, it is interesting

here to rationalize this signal-to-noise improvement factor in order to disentangle the different contributions. On one hand, comparing the noise level at 40 K versus 100 K, we observe a reduction of about x1.2. On the other hand, lowering the temperature from 100 K to 40 K leads to an increase of the electron Boltzmann polarization by ~2.5. Considering these two factors, it suggests that the DNP efficiency is roughly improved by a factor of ~1.6 in this case.

The polarization buildup shown in Fig. 4 (a) had to be fitted with a sum of two exponential functions at both temperatures. The short and the long components are 5.7 s (50 %), and 62 s (50 %) at 100 K, and 8.5 s (55 %) and 96 s (45 %) at 40 K. The requirement of a two-components fit is consistent with the hyperpolarization of a core-shell structure. Interestingly, both the short and long components of the buildup get slightly longer upon cooling from 100 to 40 K, while their respective weight is roughly preserved (about 1:1). Note that the long component is limited by bulk ^{1}H T_{1n} (undoped). Fig. 4 (b) shows the ^{13}C CPMAS spectrum with and without microwave irradiation for a recycling time that maximizes the sensitivity with microwave. The corresponding DNP enhancement factor is 98 at 40 K and 62 at 100 K, with 11.5 s and 8.2 s recycling time, respectively. Comparing the sensitivity, a factor of ~2.7 of improvement is observed when lowering the temperature from 100 K to 40 K. In terms of resolution, the full width at half height (FWHH) of the CO resonance is roughly identical at both temperatures. This is therefore a nice example where sensitivity is improved without compromising the resolution. Another striking observation is the large x35 of signal enhancement of the methyl groups at 40 K compared to 100 K. It is well established that the methyl rotation at 100 K makes the ^{1}H hyperpolarization by DNP challenging, and that it can also potentially interfere with CP and ^{1}H decoupling spin dynamics, resulting usually in low intensities for CH_3 signals. As suggested in Ref [85], the reduced methyl rotation below 75 K is likely to help recovering more favorable relaxation properties, which is

confirmed by our data. Lowering the sample temperature at 40 K should definitely help probing methyl-methyl long-range constraints as suggested in Ref [85].

The case of indomethacin microcrystals is very different. Indeed, the time required to hyperpolarize the particles (up to 10 s or more) is typically longer than the bulk ^{1}H T_{1n} of ~3 s at 100 K, making them difficult to polarize at 100 K, as shown in Fig. 4 (c). Interestingly, the ^{1}H polarization buildup at 100 K can be fitted using only one component of about 1.3 s. This makes sense considering the bulk ^{1}H bulk T_{1n} (undoped). In this case, we only start polarizing the outer shell of the microcrystals but diffusion of the hyperpolarization within the particle is limited by the bulk ^{1}H T_{1n}, which brings the polarization back to Boltzmann equilibrium. Remarkably, as we cool the sample down to 40 K, the ^{1}H buildup (Fig. 4 (c)) becomes bi-exponential, with a short component at 3.3 s and a longer one at 47 s (weights of 41 % and 59 %, respectively). This clearly highlights that hyperpolarization can now be transferred beyond the outer shell of the particles, as a direct consequence of a longer bulk ^{1}H T_{1n} of indomethacin microcrystals at 40 K. Finally, Fig. 4 (d) shows the ^{13}C CPMAS spectrum of indomethacin with and without microwave irradiation at 40 K for a recycling time of 5 s that maximizes the sensitivity with microwave. The corresponding DNP enhancement factor is 23, to be compared to the DNP enhancement factor of 3 at 100 K with 1.8 s recycling. Overall, this translates into an improvement in sensitivity of x5 and or in time-savings of x25 when going from 100 K to 40 K, using cAsymPol-POK as polarizing agent.

Multidimensional experiments at 40 K

After discussing the improved sensitivity that is achieved on organic microcrystals, we also show that our closed-loop He cycle can be used to record multidimensional experiments that requires stable spinning, double/triple channel irradiation and high power H/X/Y pulses. The experiments shown in Fig. 5 were performed on diluted tri-peptide U-^{13}C,^{15}N-N-Formylmethionyl-leucyl-phenylalanine (*f*-MLF). With a bulk ^{1}H T_{1n} of ~3 s at 100 K, this microcrystalline system is also challenging to polarize. Similarly, to the indomethacin case, a drastic improvement in SNR of a factor of 6 is obtained by hyperpolarizing this sample at 40 K compared to 100 K, using cAsymPol-POK as polarizing agents. The polarization buildup at 40 K is bi-exponential with components at 3.6 s (40 %) and 20 s (60 %).

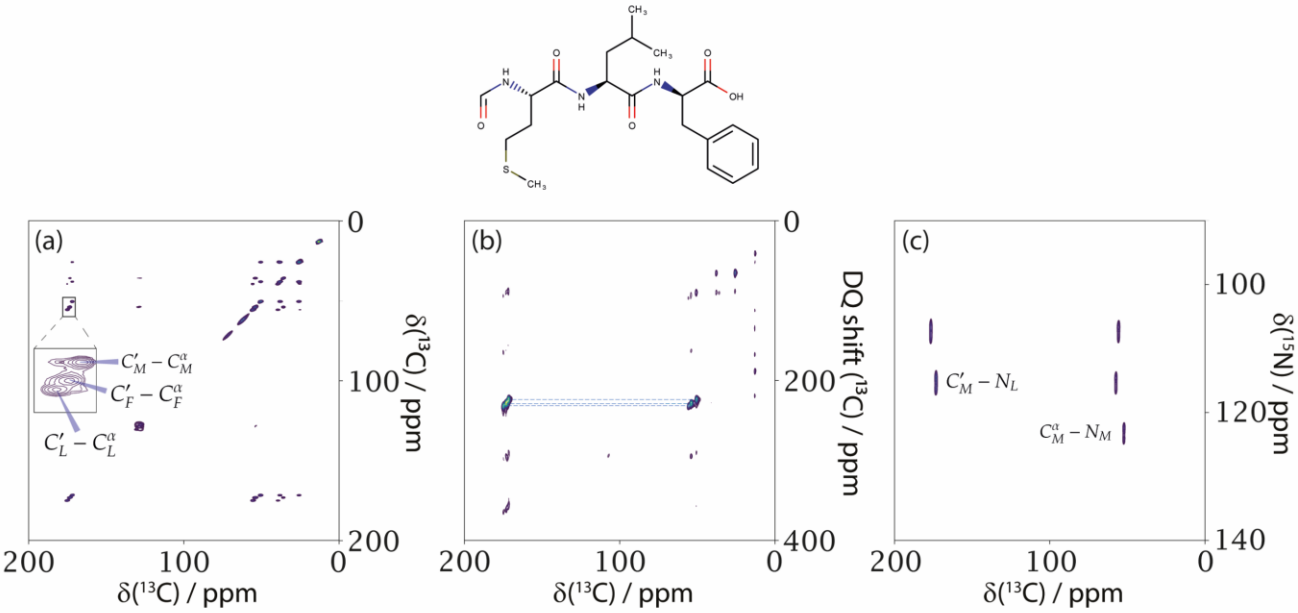

Figure 5. Different 2D experiments on the *f*-MLF sample. (a) 2D ^{13}C-^{13}C DARR spectrum obtained in 49 minutes with 20 ms of mixing time. The inset shows intra- (labelled) and inter-residue cross peaks. (b) DQ-SQ spectrum using SR26 with STiC phase shifts. It was acquired in 1 hr 42 min with 4.77 ms of total mixing time. (c) Triple-resonance z-filtered TEDOR experiment with excellent sensitivity obtained in 1 h 14 min, with a mixing time of 2.2 ms.

Fig. 5 (a) shows a 2D ^{13}C-^{13}C DARR correlation spectrum obtained with 20 ms of mixing time. As shown in the inset, the spectrum is dominated by intra-molecular cross peaks (e.g. $C_M' - C_M^\alpha$

, $C_F' - C_M^\alpha$, and $C_L' - C_L^\alpha$ for the region considered in the inset), but inter-residue cross peaks (e.g. $C_M' - C_L^\alpha$ and $C_L' - C_F^\alpha$) are also visible at smaller intensity because of the isotopic dilution of the sample. The well-resolved data stresses two important points: (a) the magic angle can be set very accurately given the resolution of the carbonyl lines, (b) high power ^{1}H decoupling can be applied during 30 ms (or more) without any sign of arcing, enabling the good resolution achieved in both dimensions.

To further highlight the excellent spinning stability and RF performance of the probe, we report in Fig. 5 (b) a 2D DQ-SQ correlation experiment required at 6.7 kHz MAS using SR26 [67] combined with STiC phase shift [68]. The latter alleviates the need to rotor-synchronize evolution in the indirect dimension. This yields clean 2D data, where the spectral width in the indirect dimension can be chosen sufficiently large to avoid signal folding. The very good quality of the 2D spectrum and the absence of artefact are the direct consequence of the excellent spinning stability and RF performance of the probe. Finally, we report a triple resonance zf-TEDOR experiments in Fig. 5 (c) employing 15 ms of 75 kHz ^{1}H decoupling. The correlations seen in the 2D correspond to N-Cα and N-C' transfer over one-bond.

CONCLUSIONS

In this work, we have described a sustainable and cost-effective approach to cryogenic Helium spinning. The system is based around a new He spinning MAS-DNP probe, a powerful counter-flow heat exchanger (95 % efficient), a single cryo-cooler and a single He compressor. The current setup allows reaching 27 K at low spinning speed (~5 kHz), and about 30-35 K at 10 kHz (in absence of microwave irradiation). Faster spinning frequencies can be achieved (up to 15 kHz at 40 K) but not reliably. Indeed, at such spinning frequencies, the drive caps often come off due to the differential thermal contraction of the rotor (zirconia) and the caps (vespel), but we are

currently working on this problem with the design of new rotor caps for faster spinning. In addition, the system is equipped with a cryogenic sample exchange capability, which allows swapping samples in minutes. Tested on organic microcrystals, we report large SNR improvements by decreasing the sample temperature from 100 to 40 K. The improvements are particularly pronounced for systems that are difficult to polarize because of their intrinsic short ^{1}H T_{1n} at 100 K. The excellent MAS stability and RF performance of the probe are illustrated with double/triple resonance 2D experiments.

Beyond the goal of performing NMR/DNP in the < 50 K regime, the Grenoble setup has been developed with a clear commitment towards cost-effectiveness and sustainability, with considerable attention paid to thermal isolation and heat transfer efficiency, to minimize cooling power requirements, footprint, power consumption and maintenance cost. The Grenoble setup has now an efficient sample insert-eject capability and will be upgraded in a next future with a second cryocooler to reach < 15 K. Overall, the Grenoble setup paves the way to a cost-effective solution for sustainable fast MAS He spinning. These advances will be combined with the development of tailored polarizing agents and should prove particularly useful for the development of very high field DNP combined for instance with cheaper solid-state sources.

AUTHOR INFORMATION

Corresponding Author

*E-mail: gael.depaepe@cea.fr

ACKNOWLEDGEMENTS

This work was supported by the French National Research Agency through CBH-EUR-GS and the Labex ARCANE (ANR-17-EURE-0003), the CDP Glyco@Alps (ANR15-IDEX-02), the project TOGETHER (ANR 19-CE29-0021), and the European Research Council (ERC-CoG-2015, No. 682895). GDP thanks Frédéric Mentink-Vigier and Daniel Lee for stimulating discussions. GDP thanks Snorri Sigurdsson for providing the cAsymPol-POK polarizing agents used in this work.

REFERENCES

[1] R. Tycko, BIOMOLECULAR SOLID STATE NMR: Advances in Structural Methodology and Applications to Peptide and Protein Fibrils, Annu. Rev. Phys. Chem. 52 (2001) 575–606.
[2] J.V. Hanna, M.E. Smith, Recent technique developments and applications of solid state NMR in characterising inorganic materials, Solid State Nucl. Magn. Reson. 38 (2010) 1–18.
[3] O. Pecher, J. Carretero-González, K.J. Griffith, C.P. Grey, Materials' Methods: NMR in Battery Research, Chem. Mater. 29 (2017) 213–242.
[4] S.E. Ashbrook, J.M. Griffin, K.E. Johnston, Recent Advances in Solid-State Nuclear Magnetic Resonance Spectroscopy, Annu. Rev. Anal. Chem. 11 (2018) 485–508.
[5] D.D. Laws, H.-M.L. Bitter, A. Jerschow, Solid-State NMR Spectroscopic Methods in Chemistry, Angew. Chem. Int. Ed. 41 (2002) 3096–3129.
[6] B. Reif, S.E. Ashbrook, L. Emsley, M. Hong, Solid-state NMR spectroscopy, Nat. Rev. Methods Primer. 1 (2021) 1–23.
[7] A.A. Shcherbakov, J. Medeiros-Silva, N. Tran, M.D. Gelenter, M. Hong, From Angstroms to Nanometers: Measuring Interatomic Distances by Solid-State NMR, Chem. Rev. 122 (2022) 9848–9879.
[8] F.-X. Theillet, In-Cell Structural Biology by NMR: The Benefits of the Atomic Scale, Chem. Rev. 122 (2022) 9497–9570.
[9] A.J. Pell, G. Pintacuda, C.P. Grey, Paramagnetic NMR in solution and the solid state, Prog. Nucl. Magn. Reson. Spectrosc. 111 (2019) 1–271.
[10] A. Hassan, C.M. Quinn, J. Struppe, I.V. Sergeyev, C. Zhang, C. Guo, B. Runge, T. Theint, H.H. Dao, C.P. Jaroniec, M. Berbon, A. Lends, B. Habenstein, A. Loquet, R. Kuemmerle, B. Perrone, A.M. Gronenborn, T. Polenova, Sensitivity boosts by the CPMAS CryoProbe for challenging biological assemblies, J. Magn. Reson. 311 (2020) 106680.
[11] R. Tycko, NMR at Low and Ultra-Low Temperatures, Acc. Chem. Res. 46 (2013) 1923–1932.
[12] M. Concistrè, O.G. Johannessen, E. Carignani, M. Geppi, M.H. Levitt, Magic-Angle Spinning NMR of Cold Samples, Acc. Chem. Res. 46 (2013) 1914–1922.
[13] A.W. Overhauser, Polarization of Nuclei in Metals, Phys. Rev. 92 (1953) 411–415.
[14] J.I. Kaplan, Spin Resonance in Metals as a Function of the Overhauser Effect, Phys. Rev. 99 (1955) 1322–1323.

[15] T.R. Carver, C.P. Slichter, Experimental Verification of the Overhauser Nuclear Polarization Effect, Phys. Rev. 102 (1956) 975–980.
[16] D.A. Hall, D.C. Maus, G.J. Gerfen, S.J. Inati, L.R. Becerra, F.W. Dahlquist, R.G. Griffin, Polarization-Enhanced NMR Spectroscopy of Biomolecules in Frozen Solution, Science. 276 (1997) 930–932.
[17] R.G. Griffin, T.F. Prisner, High field dynamic nuclear polarization—the renaissance, Phys. Chem. Chem. Phys. 12 (2010) 5737–5740.
[18] A.B. Barnes, G. De Paëpe, P.C.A. van der Wel, K.-N. Hu, C.-G. Joo, V.S. Bajaj, M.L. Mak-Jurkauskas, J.R. Sirigiri, J. Herzfeld, R.J. Temkin, R.G. Griffin, High-Field Dynamic Nuclear Polarization for Solid and Solution Biological NMR, Appl. Magn. Reson. 34 (2008) 237–263.
[19] A. Lesage, M. Lelli, D. Gajan, M.A. Caporini, V. Vitzthum, P. Miéville, J. Alauzun, A. Roussey, C. Thieuleux, A. Mehdi, G. Bodenhausen, C. Copéret, L. Emsley, Surface enhanced NMR spectroscopy by dynamic nuclear polarization, J. Am. Chem. Soc. 132 (2010) 15459–15461.
[20] D. Lee, H. Takahashi, A.S.L. Thankamony, J.-P. Dacquin, M. Bardet, O. Lafon, G.D. Paëpe, Enhanced Solid-State NMR Correlation Spectroscopy of Quadrupolar Nuclei Using Dynamic Nuclear Polarization, J. Am. Chem. Soc. 134 (2012) 18491–18494.
[21] A.J. Rossini, A. Zagdoun, M. Lelli, A. Lesage, C. Copéret, L. Emsley, C. Coperet, L. Emsley, Dynamic Nuclear Polarization Surface Enhanced NMR Spectroscopy, Acc. Chem. Res. 46 (2013) 1942–1951.
[22] Q.Z. Ni, E. Daviso, T.V. Can, E. Markhasin, S.K. Jawla, T.M. Swager, R.J. Temkin, J. Herzfeld, R.G. Griffin, High Frequency Dynamic Nuclear Polarization, Acc. Chem. Res. 46 (2013) 1933–1941.
[23] D. Lee, S. Hediger, G. De Paëpe, Is solid-state NMR enhanced by dynamic nuclear polarization?, Solid State Nucl. Magn. Reson. 66–67 (2015) 6–20.
[24] D. Gauto, O. Dakhlaoui, I. Marin-Montesinos, S. Hediger, G. De Paëpe, Targeted DNP for biomolecular solid-state NMR, Chem. Sci. 12 (2021) 6223–6237.
[25] R.W. Hooper, B.A. Klein, V.K. Michaelis, Dynamic Nuclear Polarization (DNP) 101: A New Era for Materials, Chem. Mater. 32 (2020) 4425–4430.
[26] W.Y. Chow, G. De Paëpe, S. Hediger, Biomolecular and Biological Applications of Solid-State NMR with Dynamic Nuclear Polarization Enhancement, Chem. Rev. 122 (2022) 9795–9847.
[27] T. Biedenbänder, V. Aladin, S. Saeidpour, B. Corzilius, Dynamic Nuclear Polarization for Sensitivity Enhancement in Biomolecular Solid-State NMR, Chem. Rev. 122 (2022) 9738–9794.
[28] K.-N. Hu, G.T. Debelouchina, A.A. Smith, R.G. Griffin, Quantum mechanical theory of dynamic nuclear polarization in solid dielectrics., J. Chem. Phys. 134 (2011) 125105.
[29] K.R. Thurber, R. Tycko, Theory for cross effect dynamic nuclear polarization under magic-angle spinning in solid state nuclear magnetic resonance: The importance of level crossings, J. Chem. Phys. 137 (2012) 084508.
[30] Y. Hovav, A. Feintuch, S. Vega, Theoretical aspects of Dynamic Nuclear Polarization in the solid state - the cross effect., J Magn Reson. 214 (2012) 29–41.
[31] A. Karabanov, G. Kwiatkowski, W. Köckenberger, Spin dynamic simulations of solid effect DNP: the role of the relaxation superoperator, Mol. Phys. 112 (2014) 1838–1854.

[32] K.R. Thurber, R. Tycko, Perturbation of nuclear spin polarizations in solid state NMR of nitroxide-doped samples by magic-angle spinning without microwaves., J. Chem. Phys. 140 (2014) 184201.
[33] F. Mentink-Vigier, Ü. Akbey, H. Oschkinat, S. Vega, A. Feintuch, Theoretical aspects of Magic Angle Spinning - Dynamic Nuclear Polarization, J. Magn. Reson. 258 (2015) 102–120.
[34] F. Mentink-Vigier, S. Paul, D. Lee, A. Feintuch, S. Hediger, S. Vega, G. De Paëpe, Nuclear depolarization and absolute sensitivity in magic-angle spinning cross effect dynamic nuclear polarization, Phys. Chem. Chem. Phys. 17 (2015) 21824–21836.
[35] F. Mentink-Vigier, S. Vega, G. De Paëpe, Fast and accurate MAS–DNP simulations of large spin ensembles, Phys. Chem. Chem. Phys. 19 (2017) 3506–3522.
[36] F. Mentink Vigier, A.-L. Barra, J. van Tol, S. Hediger, D. Lee, G. De Paëpe, De novo prediction of cross-effect efficiency for magic angle spinning dynamic nuclear polarization, Phys. Chem. Chem. Phys. 18 (2019) 1–636.
[37] F.A. Perras, M. Pruski, Large-scale ab initio simulations of MAS DNP enhancements using a Monte Carlo optimization strategy, J. Chem. Phys. 149 (2018) 154202.
[38] M. Rosay, M. Blank, F. Engelke, Instrumentation for solid-state dynamic nuclear polarization with magic angle spinning NMR, J. Magn. Reson. 264 (2016) 88–98.
[39] D. Lee, E. Bouleau, P. Saint-Bonnet, S. Hediger, G. De Paëpe, Ultra-low temperature MAS-DNP, J. Magn. Reson. 264 (2016) 116–124.
[40] Y. Matsuki, T. Fujiwara, Cryogenic Platforms and Optimized DNP Sensitivity, in: eMagRes, John Wiley & Sons, Ltd, 2018: pp. 9–24.
[41] F.J. Scott, E.P. Saliba, B.J. Albert, N. Alaniva, E.L. Sesti, C. Gao, N.C. Golota, E.J. Choi, A.P. Jagtap, J.J. Wittmann, M. Eckardt, W. Harneit, B. Corzilius, S. Th. Sigurdsson, A.B. Barnes, Frequency-agile gyrotron for electron decoupling and pulsed dynamic nuclear polarization, J. Magn. Reson. 289 (2018) 45–54.
[42] K.-N. Hu, Polarizing agents and mechanisms for high-field dynamic nuclear polarization of frozen dielectric solids, Solid State Nucl. Magn. Reson. 40 (2011) 31–41.
[43] K.-N. Hu, H. Yu, T.M. Swager, R.G. Griffin, Dynamic Nuclear Polarization with Biradicals, J. Am. Chem. Soc. 126 (2004) 10844–10845.
[44] S. Hediger, D. Lee, F. Mentink-Vigier, G. De Paëpe, MAS-DNP Enhancements: Hyperpolarization, Depolarization, and Absolute Sensitivity, eMagRes. 7 (2018) 105–116.
[45] G. Menzildjian, J. Schlagnitweit, G. Casano, O. Ouari, D. Gajan, A. Lesage, Polarizing agents for efficient high field DNP solid-state NMR spectroscopy under magic-angle spinning: from design principles to formulation strategies, Chem. Sci. 14 (2023) 6120–6148.
[46] A. Zagdoun, G. Casano, O. Ouari, G. Lapadula, A.J. Rossini, M. Lelli, M. Baffert, D. Gajan, L. Veyre, W.E. Maas, M. Rosay, R.T. Weber, C. Thieuleux, C. Coperet, A. Lesage, P. Tordo, L. Emsley, A Slowly Relaxing Rigid Biradical for Efficient Dynamic Nuclear Polarization Surface-Enhanced NMR Spectroscopy: Expeditious Characterization of Functional Group Manipulation in Hybrid Materials, J. Am. Chem. Soc. 134 (2012) 2284–2291.
[47] C. Sauvée, M. Rosay, G. Casano, F. Aussenac, R.T. Weber, O. Ouari, P. Tordo, Highly Efficient, Water-Soluble Polarizing Agents for Dynamic Nuclear Polarization at High Frequency, Angew. Chem. Int. Ed. 52 (2013) 10858–10861.
[48] G. Mathies, M.A. Caporini, V.K. Michaelis, Y. Liu, K.-N. Hu, D. Mance, J.L. Zweier, M. Rosay, M. Baldus, R.G. Griffin, Efficient Dynamic Nuclear Polarization at 800 MHz / 527 GHz with Trityl-nitroxide Biradicals, Angew. Chem. Int. Ed Engl. 54 (2015) 11770–11774.

643 [49] D. Wisser, G. Karthikeyan, A. Lund, Alicia Lund, G. Casano, Hakim Karoui, H. Karoui, M.
644 Yulikov, G. Menzildjian, A.C. Pinon, A. Purea, F. Engelke, S.R. Chaudhari, D.J. Kubicki,
645 A.J. Rossini, I.B. Moroz, D. Gajan, C. Copéret, G. Jeschke, M. Lelli, L. Emsley, A. Lesage,
646 O. Ouari, O. Ouari, BDPA-Nitroxide Biradicals Tailored for Efficient Dynamic Nuclear
647 Polarization Enhanced Solid-State NMR at Magnetic Fields up to 21.1 T., J. Am. Chem. Soc.
648 140 (2018) 13340–13349.
649 [50] F. Mentink-Vigier, I. Marin-Montesinos, A.P. Jagtap, T. Halbritter, J. Van Tol, S. Hediger,
650 D. Lee, S.T. Sigurdsson, G. De Paëpe, Computationally Assisted Design of Polarizing Agents
651 for Dynamic Nuclear Polarization Enhanced NMR: The AsymPol Family, J. Am. Chem. Soc.
652 140 (2018) 11013–11019.
653 [51] A. Lund, G. Casano, G. Menzildjian, M. Kaushik, G. Stevanato, M. Yulikov, R. Jabbour, D.
654 Wisser, M. Renom-Carrasco, C. Thieuleux, F. Bernada, H. Karoui, D. Siri, M. Rosay, I.V.
655 Sergeyev, D. Gajan, M. Lelli, L. Emsley, O. Ouari, A. Lesage, TinyPols: a family of water-
656 soluble binitroxides tailored for dynamic nuclear polarization enhanced NMR spectroscopy
657 at 18.8 and 21.1 T, Chem. Sci. 68 (2020) 42–61.
658 [52] X. Cai, A. Lucini Paioni, A. Adler, R. Yao, W. Zhang, D. Beriashvili, A. Safeer, A. Gurinov,
659 A. Rockenbauer, Y. Song, M. Baldus, Y. Liu, Highly Efficient Trityl-Nitroxide Biradicals
660 for Biomolecular High-Field Dynamic Nuclear Polarization, Chem. Weinh. Bergstr. Ger. 27
661 (2021) 12758–12762.
662 [53] R. Yao, D. Beriashvili, W. Zhang, S. Li, A. Safeer, A. Gurinov, A. Rockenbauer, Y. Yang,
663 Y. Song, M. Baldus, Y. Liu, Highly bioresistant, hydrophilic and rigidly linked trityl-
664 nitroxide biradicals for cellular high-field dynamic nuclear polarization, Chem. Sci. 13
665 (2022) 14157–14164.
666 [54] R. Harrabi, T. Halbritter, F. Aussenac, O. Dakhlaoui, J. Van Tol, K.K. Damodaran, D. Lee,
667 S. Paul, S. Hediger, F. Mentink-Vigier, S.Th. Sigurdsson, G. De Paëpe, Highly Efficient
668 Polarizing Agents for MAS-DNP of Proton-Dense Molecular Solids, Angew. Chem. Int. Ed.
669 61 (2022) e202114103.
670 [55] T. Halbritter, R. Harrabi, S. Paul, J. Van Tol, D. Lee, S. Hediger, S.Th. Sigurdsson, F.
671 Mentink-Vigier, G. De Paëpe, PyrroTriPol: a semi-rigid trityl-nitroxide for high field
672 dynamic nuclear polarization, Chem. Sci. 14 (2023) 3852–3864.
673 [56] K. Thurber, R. Tycko, Low-temperature dynamic nuclear polarization with helium-cooled
674 samples and nitrogen-driven magic-angle spinning, J. Magn. Reson. 264 (2016) 99–106.
675 [57] A. Hackmann, H. Seidel, R.D. Kendrick, P.C. Myhre, C.S. Yannoni, Magic-angle spinning
676 NMR at near-liquid-helium temperatures, J. Magn. Reson. 1969. 79 (1988) 148–153.
677 [58] E.L. Sesti, N. Alaniva, P.W. Rand, E.J. Choi, B.J. Albert, E.P. Saliba, F.J. Scott, A.B. Barnes,
678 Magic angle spinning NMR below 6 K with a computational fluid dynamics analysis of fluid
679 flow and temperature gradients, J. Magn. Reson. 286 (2018) 1–9.
680 [59] Y. Matsuki, K. Ueda, T. Idehara, R. Ikeda, I. Ogawa, S. Nakamura, M. Toda, T. Anai, T.
681 Fujiwara, Helium-cooling and -spinning dynamic nuclear polarization for sensitivity-
682 enhanced solid-state NMR at 14T and 30K, J. Magn. Reson. 225 (2012) 1–9.
683 [60] Y. Matsuki, S. Nakamura, S. Fukui, H. Suematsu, T. Fujiwara, Closed-cycle cold helium
684 magic-angle spinning for sensitivity-enhanced multi-dimensional solid-state NMR, J. Magn.
685 Reson. 259 (2015) 76–81.
686 [61] E. Bouleau, P. Saint-Bonnet, F. Mentink-Vigier, H. Takahashi, J.-F. Jacquot, M. Bardet, F.
687 Aussenac, A. Purea, F. Engelke, S. Hediger, D. Lee, G. De Paëpe, Pushing NMR sensitivity

limits using dynamic nuclear polarization with closed-loop cryogenic helium sample spinning, Chem. Sci. 6 (2015) 6806–6812.
[62] C.M. Rienstra, M. Hohwy, M. Hong, R.G. Griffin, 2D and 3D 15N−13C−13C NMR Chemical Shift Correlation Spectroscopy of Solids: Assignment of MAS Spectra of Peptides, J. Am. Chem. Soc. 122 (2000) 10979–10990.
[63] K.R. Thurber, R. Tycko, Measurement of sample temperatures under magic-angle spinning from the chemical shift and spin-lattice relaxation rate of 79Br in KBr powder, J. Magn. Reson. 196 (2009) 84–87.
[64] J.J. Helmus, C.P. Jaroniec, Nmrglue: an open source Python package for the analysis of multidimensional NMR data, J. Biomol. NMR. 55 (2013) 355–367.
[65] K. Takegoshi, S. Nakamura, T. Terao, 13C–1H dipolar-assisted rotational resonance in magic-angle spinning NMR, Chem. Phys. Lett. 344 (2001) 631–637.
[66] C.P. Jaroniec, C. Filip, R.G. Griffin, 3D TEDOR NMR Experiments for the Simultaneous Measurement of Multiple Carbon−Nitrogen Distances in Uniformly 13 C, 15 N-Labeled Solids, J. Am. Chem. Soc. 124 (2002) 10728–10742.
[67] D.H. Brouwer, P.E. Kristiansen, C.A. Fyfe, M.H. Levitt, Symmetry-Based 29 Si Dipolar Recoupling Magic Angle Spinning NMR Spectroscopy: A New Method for Investigating Three-Dimensional Structures of Zeolite Frameworks, J. Am. Chem. Soc. 127 (2005) 542–543.
[68] K. Märker, S. Hediger, G. De Paëpe, Efficient 2D double-quantum solid-state NMR spectroscopy with large spectral widths, Chem. Commun. 53 (2017) 9155–9158.
[69] Y. Matsuki, S. Nakamura, F. Hobo, Y. Endo, H. Takahashi, H. Suematsu, T. Fujiwara, Cryogenic signal amplification combined with helium-temperature MAS DNP toward ultimate NMR sensitivity at high field conditions, J. Magn. Reson. 335 (2022) 107139.
[70] M. Rosay, L. Tometich, S. Pawsey, R. Bader, R. Schauwecker, M. Blank, P.M. Borchard, S.R. Cauffman, K.L. Felch, R.T. Weber, R.J. Temkin, R.G. Griffin, W.E. Maas, Solid-state dynamic nuclear polarization at 263 GHz: spectrometer design and experimental results, Phys. Chem. Chem. Phys. 12 (2010) 5850.
[71] H. Takahashi, S. Hediger, G. De Paëpe, Matrix-free dynamic nuclear polarization enables solid-state NMR 13C–13C correlation spectroscopy of proteins at natural isotopic abundance, Chem. Commun. 49 (2013) 9479.
[72] K. Märker, S. Paul, C. Fernández-De-Alba, D. Lee, J.-M. Mouesca, S. Hediger, G. De Paëpe, Welcoming natural isotopic abundance in solid-state NMR: probing π-stacking and supramolecular structure of organic nanoassemblies using DNP, Chem. Sci. 8 (2017) 974–987.
[73] K. Märker, M. Pingret, J.-M. Mouesca, D. Gasparutto, S. Hediger, G. De Paëpe, A New Tool for NMR Crystallography: Complete ^{13} C/ ^{15} N Assignment of Organic Molecules at Natural Isotopic Abundance Using DNP-Enhanced Solid-State NMR, J. Am. Chem. Soc. 137 (2015) 13796–13799.
[74] D. Lee, N.T. Duong, O. Lafon, G. De Paëpe, Primostrato solid-state NMR enhanced by dynamic nuclear polarization: Pentacoordinated Al3+ ions are only located at the surface of hydrated γ-alumina, J. Phys. Chem. C. 118 (2014) 25065–25076.
[75] M. Dekhil, G. Mollica, T.T. Bonniot, F. Ziarelli, P. Thureau, S. Viel, Determining carbon–carbon connectivities in natural abundance organic powders using dipolar couplings, Chem. Commun. 52 (2016) 8565–8568.

[76] G. Mollica, M. Dekhil, F. Ziarelli, P. Thureau, S. Viel, Quantitative Structural Constraints for Organic Powders at Natural Isotopic Abundance Using Dynamic Nuclear Polarization Solid-State NMR Spectroscopy, Angew. Chem. Int. Ed. 54 (2015) 6028–6031.
[77] Y. Matsuki, T. Sugishita, T. Fujiwara, Surface-Only Spectroscopy for Diffusion-Limited Systems Using Ultra-Low-Temperature DNP MAS NMR at 16.4 T, J. Phys. Chem. C. 124 (2020) 18609–18614.
[78] K.R. Thurber, A. Potapov, W.-M. Yau, R. Tycko, Solid state nuclear magnetic resonance with magic-angle spinning and dynamic nuclear polarization below 25K, J. Magn. Reson. 226 (2013) 100–106.
[79] P.C.A. van der Wel, K.-N. Hu, J. Lewandowski, R.G. Griffin, Dynamic Nuclear Polarization of Amyloidogenic Peptide Nanocrystals: GNNQQNY, a Core Segment of the Yeast Prion Protein Sup35p, J. Am. Chem. Soc. 128 (2006) 10840–10846.
[80] A.J. Rossini, A. Zagdoun, F. Hegner, M. Schwarzwälder, D. Gajan, C. Copéret, A. Lesage, L. Emsley, Dynamic Nuclear Polarization NMR Spectroscopy of Microcrystalline Solids, J. Am. Chem. Soc. 134 (2012) 16899–16908.
[81] H. Takahashi, B. Viverge, D. Lee, P. Rannou, G. De Paëpe, Towards Structure Determination of Self-Assembled Peptides Using Dynamic Nuclear Polarization Enhanced Solid-State NMR Spectroscopy, Angew. Chem. Int. Ed. 52 (2013) 6979–6982.
[82] R. Thakur, N. Kurur, P. Madhu, Swept-frequency two-pulse phase modulation for heteronuclear dipolar decoupling in solid-state NMR, Chem. Phys. Lett. 426 (2006) 459–463.
[83] S. Paul, N.D. Kurur, P.K. Madhu, On the choice of heteronuclear dipolar decoupling scheme in solid-state NMR, J. Magn. Reson. 207 (2010) 140–148.
[84] G. Metz, X.L. Wu, S.O. Smith, Ramped-Amplitude Cross Polarization in Magic-Angle-Spinning NMR, J. Magn. Reson. A. 110 (1994) 219–227.
[85] Q.Z. Ni, E. Markhasin, T.V. Can, B. Corzilius, K.O. Tan, A.B. Barnes, E. Daviso, Y. Su, J. Herzfeld, R.G. Griffin, Peptide and Protein Dynamics and Low-Temperature/DNP Magic Angle Spinning NMR, J. Phys. Chem. B. 121 (2017) 4997–5006.

For Table of Contents Only